Characterisation of plasma synthetic jet actuators in quiescent flow

Zong, Haohua; Kotsonis, Marios

DOI
10.1088/0022-3727/49/33/335202

Publication date
2016

Document Version
Accepted author manuscript

Published in
Journal of Physics D: Applied Physics

Characterisation of Plasma Synthetic Jet Actuators in Quiescent Flow

Haohua Zong* and Marios Kotsonis

Faculty of Aerospace Engineering, Delft University of Technology, Delft 2629 HS, Netherlands

Abstract: An experimental characterisation study of a large-volume three-electrode Plasma Synthetic Jet Actuator (PSJA) is presented. A sequential discharge power supply system is used to activate the PSJA. Phase-locked planar Particle Image Velocimetry (PIV) and time-resolved Schlieren imaging are used to characterise the evolution of the induced flow field in quiescent flow conditions. The effect of orifice diameter is investigated. Results indicate three distinct features of the actuator-induced flow field. These are the initial shock waves, the high speed jet and vortex rings. Two types of shock waves with varied intensities, namely a strong shock wave and a weak shock wave, are issued from the orifice shortly after the ignition of the discharge.. Subsequently, emission of a high speed jet is observed, reaching velocities up to 130 m/s. Pronounced oscillation of the exit velocity is caused by the periodical behaviour of capacitive discharge, which also lead to the formation of vortex ring trains. Orifice diameter has no influence on the jet acceleration stage and the peak exit velocity. However, a large orifice diameter results in a rapid decline of exit velocity and thus a short jet duration time. Vortex ring propagation velocities are measured at peak values ranging from 55 m/s to 70 m/s. In the case of 3 mm orifice diameter, trajectory of the vortex ring severely deviates from the actuator axis of symmetry. The development of this asymmetry in the flow field is attributed to asymmetry in the electrode configuration.

Key words: plasma; synthetic jet; actuator; flow control; flow field; characterisetion

**Corresponding email: H.zhong-1@tudelft.nl*

I. INTRODUCTION

In the last 15 years, plasma-based flow control has received overwhelming attention from the flow control community, due to attractive features such as non-moving components, high bandwidth, and fast response [1-2]. Several studies have demonstrated successful application of this technology for control of flow separation, boundary layer transition, shock wave/boundary layer interaction, compressor stability extension etc. [3-6]. Plasma Synthetic Jet Actuators (PSJA) represent a novel implementation of plasma actuator, which integrates the low energy consumption of surface dielectric barrier discharge actuator and the high actuation intensity of surface arc discharge actuator [7-8]. Since its introduction in 2003, PSJA has become an emerging research topic in high speed flow control, and has been widely tested in concepts of shock wave manipulation, shock wave/boundary layer interaction control, airfoil trailing edge separation control, noise mitigation and flight control [8-14].

Typical geometrical configuration of PSJA includes a cavity, two electrodes and a jet exit. The basic working principle of PSJA consists of three stages: energy deposition stage, jet stage and refresh stage. During the energy deposition stage, a pulsed arc/spark is formed in the cavity and the cavity gas is pressurized due to fast heating. In the jet stage a high speed jet is issued out of the cavity driven by the pressure difference across the exit throat, while the cavity pressure gradually drops. Finally, the jet terminates and the refresh stage begins. High-density and low-temperature air is sucked into the cavity and mixed with the residual gas.

Based on the content, research on the plasma synthetic jet can be roughly divided into two categories, actuator characterisation and flow control applications. The purpose of characterisation studies is to better understand the influence of various operational parameters on PSJA performance, and thus instruct the optimal design of the actuator and the power supply. Essentially, PSJA is an energy conversion system, converting the provided electrical energy to the gas mechanical energy in the form of both jet kinetic energy and shock wave pressure energy. Parameters influencing PSJA performance can be electrical parameters (input parameters), geometrical parameters (system structural parameters), and atmospheric parameters (working medium parameters).

Electrical parameters mainly include discharge energy, discharge frequency and discharge waveform. Among these, discharge energy has a dominant influence on PSJA performance [14-16]. With increasing discharge energy, peak jet velocity, jet duration time, pulsed thrust (impulse), and jet-affected area, increase respectively. The induced flow field features change from appearance of only weak shock waves without jet (low energy) to the coexistence of strong shock waves, strong jet and a train of vortex rings (high energy) [14-20]. However, high discharge energy will result in a high-temperature spark/arc with low time-averaged arc resistance, leading to declining discharge efficiency [21-22]. As the actuation frequency increases, the averaged jet velocity, the expelled mass per period, and the cavity density drop due to the reduced refresh time and the accumulated cavity temperature [16, 23-25]. Commonly adopted discharge types consist of capacitive discharge, inductive discharge, nanosecond pulse discharge, and pulsed DC discharge. Jets induced by the capacitive discharge demonstrate higher peak jet velocity but shorter jet duration [26] compared with inductive discharge type. By comparing the experimental pulsed thrust with that obtained from analytical models, heating efficiency of the capacitive discharge has been determined to be less than 10%, and inversely proportional to the amount of energy deposition [27-29]. In contrast, nanosecond pulse discharge is reported to have a significantly higher heating efficiency (~60%), and decrease of the rising rate benefits the jet intensity improvement [30-31].

Nevertheless, due to the typically low discharge energy (<20 mJ) associated with nanosecond pulse discharge, the latter cannot be used to feed large volume (>1000 mm^3) PSJA. For pulsed DC discharge, the discharge current, duration and frequency can be easily adjusted by high-voltage power switches. A disadvantage of this approach is the larger portion of electrical energy dissipated by the current-limiting resistor, leading to a low discharge efficiency [20, 25].

Important geometrical parameters for PSJA consist of cavity volume, exit orifice diameter, electrode distance, and discharge location. For constant discharge energy, increasing cavity volume leads to decrease of both the peak jet velocity and the total impulse [32]. Similarly, large exit orifice diameter results in a short jet duration time, but high repetitive working performance as defined by Zong et al. [23, 33]. With the energy deposition kept constant and the electrode distance increasing, the jet duration time and the peak jet velocity improve significantly due to the augmented heating volume [33]. Discharge location near the exit leads to a stronger oscillation of the exit velocity but shorter duty cycle, compared with discharge location far from the exit [34]. Additionally, the exit throat length has no influence on the single-pulse performance of PSJA, while the repetitive working performance is inversely proportional to the throat length. Finally, the influence of atmospheric parameters has received limited attention, with only the effects of ambient pressure present in existing literature. When the pressure decreases from 1 atm to 0.1 atm, mass flux of the plasma jet always decreases, but strength of the precursor shock wave shows a local maximum at 0.6 atm [35].

Flow control application studies of PSJA have typically focused on energetic turbulent flows. The produced jet by the pulsed DC discharge (discharge energy: 30 mJ) was found able to penetrate 1.5 boundary-layer thicknesses in a Mach 3 cross-flow [25]. A maximum shock wave turning angle of 5º is observed in a Mach 1.5 flow, with a discharge energy between 1.26 J and 2.34 J [10]. In an application for control of SWBLI (discharge energy: 22 mJ-49 mJ), the pressure fluctuation associated with the unsteady large-scale motion of the separated flow, showed a 30% decrease in amplitude, and the distance between the separation line and the compression ramp corner was reduced up to 40% [8-9]. Trailing edge separation was effectively delayed on a NACA 0015 model with the use of 20 PSJA. 19% drag reduction was obtained, at 40 m/s freestream velocity (Reynolds number: 1.3×10^6)[12].

Overall, the majority of existing work is focused on the influence of actuation parameters on the macroscopic performance of the jet (jet velocity, jet duration etc.). Currently few studies are concerned with the evolution of detailed flow structures (vortex rings, shock waves) pertinent to this type of actuators [19, 36-38]. However, the evolution of these structures in quiescent flow conditions is crucial towards understanding the interaction mechanism between PSJA and external flows. Additionally, the influence of geometrical parameters has so far received limited attention compared to electrical parameters such as deposited energy. Geometry effects, should also be studied to support the optimal design of PSJA in flow control applications. The present paper investigates the influence of orifice diameter on characteristics of PSJA in quiescent flows, based on high-speed Schlieren imaging system and phase-locked PIV system. In Section II, main experimental setups, including a three-electrode large-volume PSJA and a sequential discharge power supply, are introduced systematically. Then, in Section III and Section IV, Schlieren results and PIV results are present successively. Detailed evolutions of flow field structures are analysed, and influence of orifice diameter is studied.

II. EXPERIMETNAL SETUP

A. Actuator

A three-electrode configuration actuator is adopted, as shown in Fig. 1 (a). The PSJA actuator is cylindrical and consists of a ceramic cavity, three electrodes and a metal lid. The cavity is made of glass ceramic (MACOR), with diameter of 12 mm and height of 15 mm resulting in a cavity volume of 1696 mm^3. Four uniformly spaced holes with a diameter of 1.2 mm are drilled in the circumferential direction, in a plane located 7.5 mm from the cavity bottom. Three of the holes accommodate tungsten needles, which are configured as anode, cathode and trigger electrode, respectively. The remaining hole is connected with a metal capillary tube (inner diameter of 0.6 mm) used for the supply of seeding particles necessary for the PIV measurement. The metal lid can be combined together with the ceramic cavity through a step trough. A round orifice is drilled in the lid centre, to accommodate the jet exit. Centre of the jet exit is set as the coordinate origin, as shown in Fig.1 (a). Three lids with different diameters (1.5 mm, 2 mm and 3 mm) are machined, to conduct the parametric investigation. Four needle holders with screw thread, and a nylon support base, are designed to enable accurate adjustment of the distance between electrodes, as shown in Fig. 1 (b). In this study, distance from actuator axisymmetry axis (y) to anode, cathode and trigger electrode, is fixed as 1 mm, 2 mm and 0.5 mm, respectively.

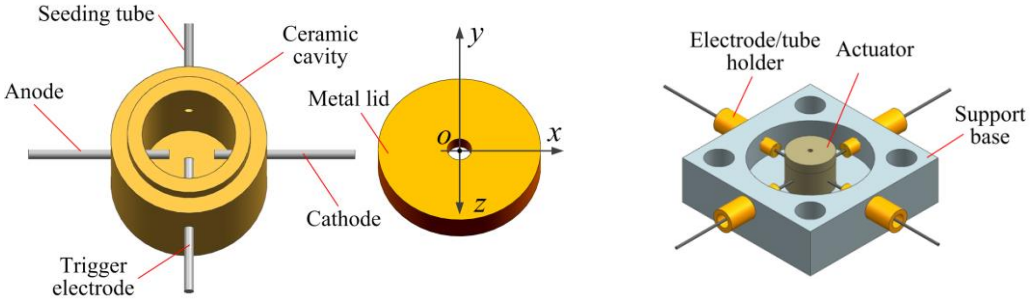

(a) Actuator components and coordinate system (b) Support base

Fig. 1 Actuator structure and used coordinate system

B. Power supply system

A capacitive discharge was chosen to realize the large energy deposition necessary for the utilised PSJA. A high-voltage amplifier, in conjunction with several electrical components, constitutes the power supply system, as shown in Fig. 2. Compared with the system used in Zong et al. [17], this power supply system is more simple in structure since the HV amplifier realizes both triggering function and charging function.

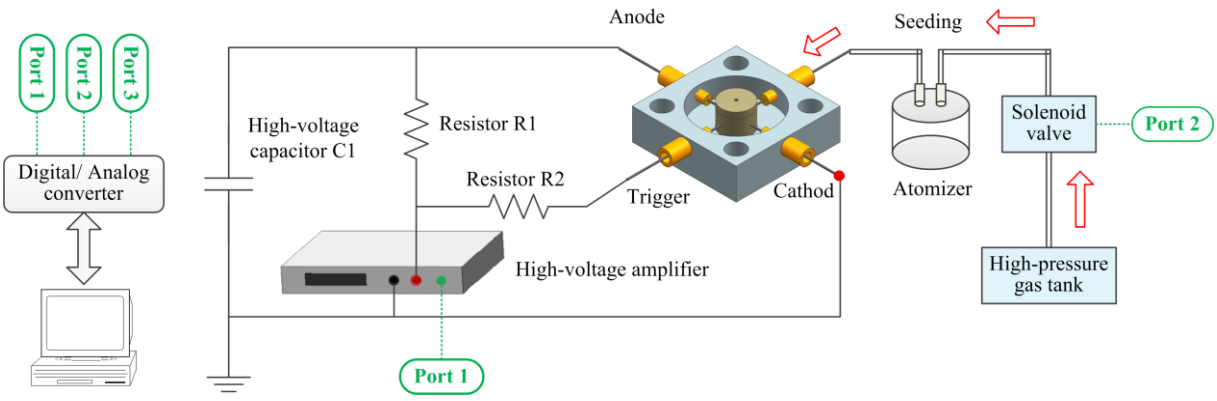

Fig. 2 Power supply system and PIV seeding system

The working process of the system is as follows. First, the high-voltage amplifier (Trek Model 20/20C), outputs a high-voltage charge pulse (amplitude: 2.5 kV, pulse width: 1600 ms) to charge a high-voltage capacitor C1 (withstand voltage: 5 kV, capacitance: 1 μF). A large resistor R1 (200 MΩ, 100 W) is used to limit the charge current below the maximum output current (20 mA) of the high-voltage amplifier. The width of the charge pulse is determined by the characteristic time of the charging circuit, namely the product of capacitance C1 and resistance R1. Subsequently, a high-voltage trigger pulse (amplitude: 8 kV, pulse width: 100 μs), is produced just after the end of the first high-voltage pulse. The trigger pulse is established at a voltage higher than the breakdown threshold of air for the used inter-electrode distance, and thus is able to initiate the discharge. After the discharge channel is established, a strong arc discharge is formed between the anode and the cathode, and the electrical energy stored in capacitor is released as thermal energy in the cavity. A protective resistor R2 (2 kΩ, 100 W) is added between the high-voltage amplifier and the trigger electrode, to limit the discharge current back to the high-voltage amplifier. Amplification ratio of the high-voltage amplifier is 2000. The triggering and charging signal is programmed using LABVIEW, and output by a digital/analog converter (NI, cDAQ-9174). Additionally, trigger signals for the seeding system and the PIV system are also produced by the digital/analog converter. Time sequences of these trigger signals will be detailed in Section II.C.(2).

C. Measurement system

High-speed Schlieren imaging and two-component planar phase-locked PIV measurements were adopted to visualize and quantify features of the flow field. With these two techniques, density gradient information and velocity information of the jet can be obtained.

(1). Schlieren imaging setup

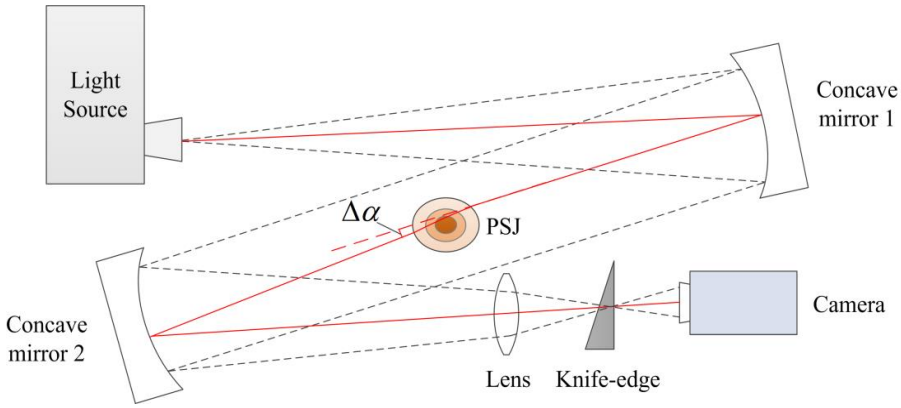

Fig. 3 Schlieren imaging system

A typical Z-type Schlieren imaging system was exploited, mainly consisting of a light source, two concave mirrors, a knife-edge and a high-speed digital camera (PCO dimax S4, 12bit, 4MPix), as shown in Fig. 3. Light rays emitted from the continuous light source were first reflected by the two concave mirrors (diameter: 30 cm, focal length: 3 m), then converged by a 250 mm spherical lens, and finally projected onto the camera sensor directly. A knife-edge was placed vertically in the focal point to increase the image contrast in the *x* direction. Schlieren images were recorded at exposure time of 1.28 μs, and frame rate of 20 kHz. To reach this sampling rate the sensor was cropped to 240×500 pixels, resulting in a scaling factor of 0.0926 mm/pixel.

(2). PIV setup

Two-component planar phase-locked PIV was performed to evaluate the flow field in the *xy* symmetry plane of the actuator (z=0 mm). The actuator was placed in a closed plexiglass box (dimensions: 1×0.5×0.5 m^3)

to ensure quiescent flow conditions. In order to solve the problem of low seeding density in jet region shown in [37], both the actuator cavity and the box are seeded with dielectric mineral oil particles (Shell Ondina, mean diameter: 1 μm), generated by an atomizer (TSI 9302). The intra-cavity seeding was controlled by a fast-switching solenoid valve (FESTO, MHJ10). The solenoid valve was kept open in between measurements and closed before and during each discharge in order to minimise influences on the developing jet. Field illumination was provided by a dual-head Nd:YAG laser (Quantel, CFR PIV-200), adopted to output two sequential laser pulses with a maximum energy of 200 mJ. The laser beam was first shaped into a sheet by two spherical and one cylindrical lenses and then cut by two knife-edges to final thickness of approximately 0.6 mm. Both the laser sheet and the actuator were kept strictly vertical to eliminate the influence of gravity on the formed jet plume. A LaVision digital CCD camera (Imager Pro LX, resolution: 3248×4872 pixels) mounted with a Nikon Micro-Nikkor 200 mm macro lens was used to record the illuminated particle images at repetition frequency of 0.5 Hz. The imaged field of view (FOV) was 34×51 mm^2, resulting in a magnification ratio of 0.71.

In order to capture the jet evolution deterministically, the separate systems such as discharge circuit, particle seeding system and PIV system, were synchronized by using Labview, working in a phase-locked mode. Detailed time sequences (Fig. 4) were as follows:

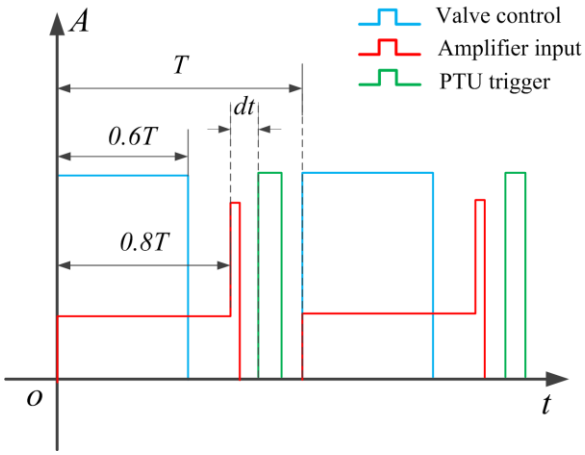

Fig. 4 Time sequence of discharge (Amplifier input), seeding valve (Valve control) and PIV acquisition (PTU trigger)

First, the solenoid valve is activated and seeding particles begin to fill the cavity. At the same time, the high-voltage capacitor is charged. In order not to interfere with the evolution of the flowfield the valve is turned off prior to the discharge initiation at 0.6*T* (1.2 s). Finally, the discharge and the Programed Timing Unit (PTU) of the PIV system are triggered with a time delay, *dt*. Note that the time delay between the discharge and the image recording will be denoted as *t* hereinafter. Time delay between the two lasers are determined by the maximum displacement of tracing particles, and is adjusted dynamically from 1 μs to 4 μs, so as to obtain a 10-15 pixel maximum displacement at each phase.

The evolution time of the synthetic jet was found to vary between 2 to 3 ms, depending on the orifice diameter. Thus, the maximum recording time was set as 3 ms for 1.5 mm orifice diameter and 2 ms for the remaining cases. The time step between subsequent phases was chosen as 50 μs or 100 μs, in order to match the Schlieren measurements. For each phase, 200 image pairs were acquired to extract first and second order statistical quantities. LaVision Davis 8.3 was used to correlate the PIV images. Final interrogation window and

overlap ratio were set as 32×32 pixels and 75%, respectively, resulting in a final spatial resolution of 12 vectors/mm.

III. SCHLIEREN IMAGING

Schlieren imaging results are presented in this section. Influence of the orifice diameter (denoted as *D*) is investigated, and vortex ring propagation velocity of PSJA is quantified.

A. Flow field evolution

Schlieren results (8-bit grayscale images) for exit orifice diameter of 3 mm are shown in Fig. 5. Note that Fig. 5 (a) is an instantaneous image, since averaging will smooth the shock wave edge. However, Fig. 5 (b-j) are conditional averaged images, to highlight the vortex and the jet structures. The number of averaged images per phase is 10, and the averaging condition is based on the wall normal position of the vortex ring at t=150 μs.

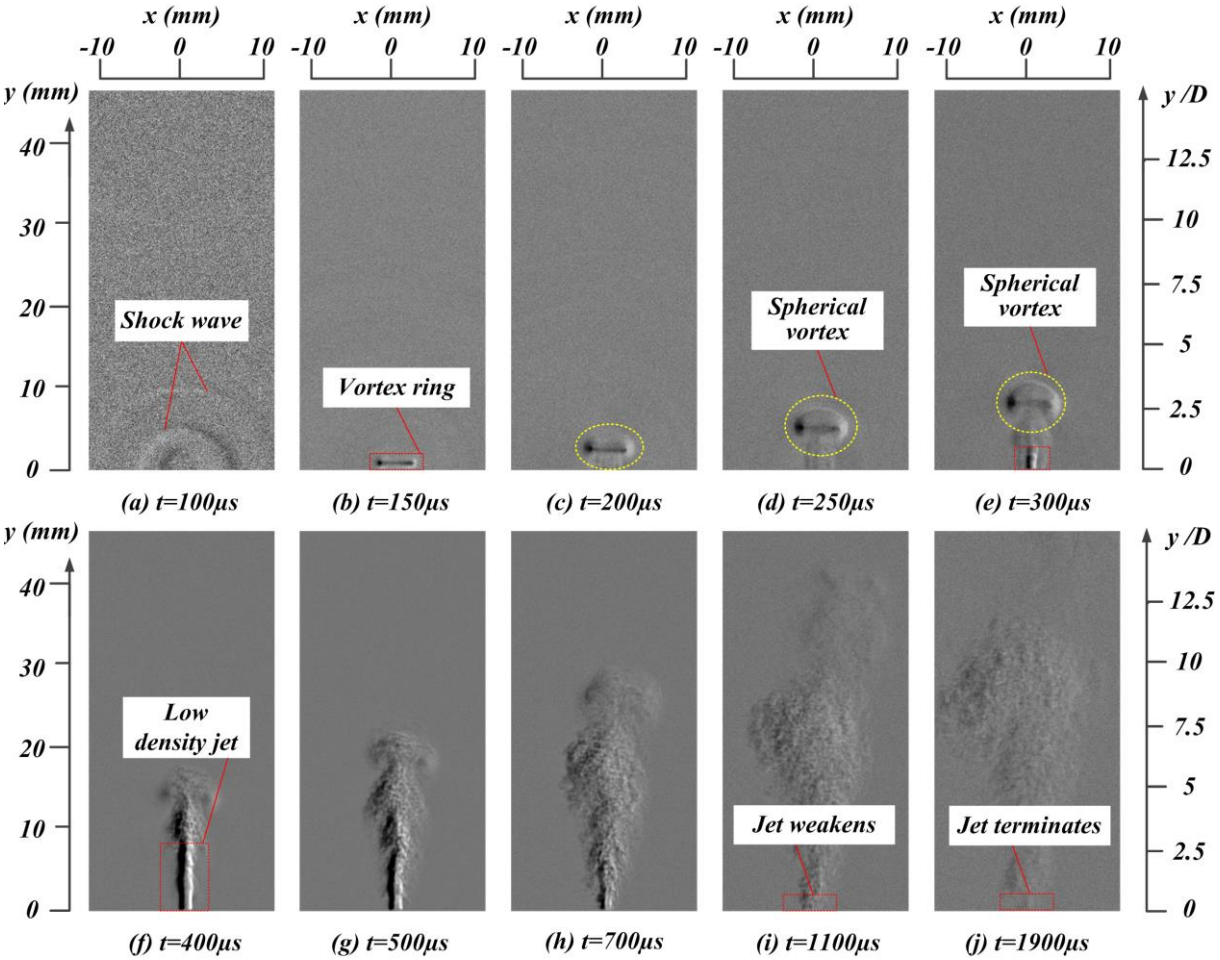

Fig. 5 Schlieren images of jet evolution for orifice diameter of 3 mm (grayscale values from 0 to 255)

At t=100 μs after the initiation of discharge, no jet is present and only several shock waves can be observed. Presence of the multiple shock waves is caused by the shock wave reflections within the cavity and the oscillation of the energy deposition [22, 33]. A coherent vortex ring sheds from the orifice at t=150 μs, due to the impulsive starting jet. After formation, the vortex ring propagates along the actuator centreline, gradually increasing in size due to entrainment of the high speed jet and surrounding air. At t=300 μs, the vortex ring evolves into a spherical shape. With the exception of the shock wave, the flow field evolution in the first 300 μs pertains to features of a conventional starting pulsed jet with a constant exit velocity [39-40]. After t = 300 μs, a

well defined jet is expelled from the cavity and the jet plume gradully grows in volume, penetrating the quiescent flow environment. Based on the grayscale level near exit, the jet weakens considerably after t=1100 μs, and terminates at t=1900 μs.

Additional to the topological evolution of the jet, another two interesting phenomena are observed. The first is the variation of the jet grayscale. Grayscale value in Schlieren images corresponds to the integration of density gradients along the *x* direction (vertical knife-edge). Between t =150 μs and t =250 μs, the observed jet has a rather small grayscale difference with the surrounding air. However, between t = 300 μs and t = 700 μs, the jet core is characterized by an intense variation in grayscale. The grayscale difference reflects the light deflection angle, and further the integral of density gradient along the light ray. It becomes evident that the initial jet has a relatively high density (close to the ambient density), while the later expelled jet is of considerably lower density and high temperature (the exit static pressure can be assumed to be ambient pressure due to the subsonic jet velocity). Note after t=700 μs, the jet body becomes less distinctive again, meaning that exit density will finally increase in jet stage. These observations confirm the simulation results in [41], where jet exit density in one period first drops sharply, then sustains a relatively low value, and finally increases. The source of the sudden change of density and temperature of the jet lies in the nonuniform heating nature of the arc discharge. During the discharge, most of the thermal energy is deposited locally in the arc discharge region, which is only a small portion of the cavity volume located approximately 7.5 mm lower than the exit orifice. This region is dominated by high pressure, high temperature and low density fluid. Pressurization of the remaining region is realized mainly by the fast propagation and reflection of arc-induced shock waves. Therefore, the initial issued jet (t < 300 μs) is comprised of relatively cool air near the exit, characterized by high density. The later issued jet (300 μs < t < 700 μs) is the low-density air directly heated by arc discharge.

The second interesting feature is the asymmetry of the jet, which isn't obvious in small orifice diameters (see Fig. 6 (j)). After t=500 μs, the front vortex ring separates from the jet body, and gradually leans in the right side during its propagation. This feature still exists, when the number of averaged images further increases to 20. This effect is further discussed in more detail in Section IV.A.(1).

Schlieren imaging results for the actuator of 2 mm diameter are shown in Fig. 6 and Fig. 7. It should be noted that Fig. 6 (a) and Fig. 7 pertain to instantaneous results, while Fig 6(b-j) to conditional averaged images.

While several features of the jet evolution are similar to the ones shown in Fig. 5, some differences are indicative of the effect of orifice diameter. Evidently the shock waves are considerably weaker at t = 100 μs in Fig. 7. As the shock wave evolution in the cavity is independent of the orifice diameter, the mechanical energy pertaining to the waves is positively proportional to the orifice diameter. Thus, a small orifice diameter results in a weak shock wave intensity. Additionally, between t=200 μs and t=300 μs, the jet core presents a pattern of alternating bright and dark regions, along the exit centreline, which is in agreement with the measurements of [19]. The observed pattern corresponds to a train of developing vortex rings. Further discussion of the underlying mechanism is provided in Section IV.B.(2). The jet duration is increased with decreasing diameter. This is intuitively expected, as the total expelled mass is mainly determined by the energy deposition. A small exit orifice diameter leads to a lower mass flow rate and finally a relatively lasting jet. Finally, a coherent vortex ring evolution can be observed in the instantaneous Schlieren images, between t=600 μs and t=1200 μs. During propagation, the vortex ring deforms while its propagation velocity remains almost the same.

Due to the low greyscale variation of Schlieren images for the case of D = 1.5 mm, no analysis of the jet evolution is performed.

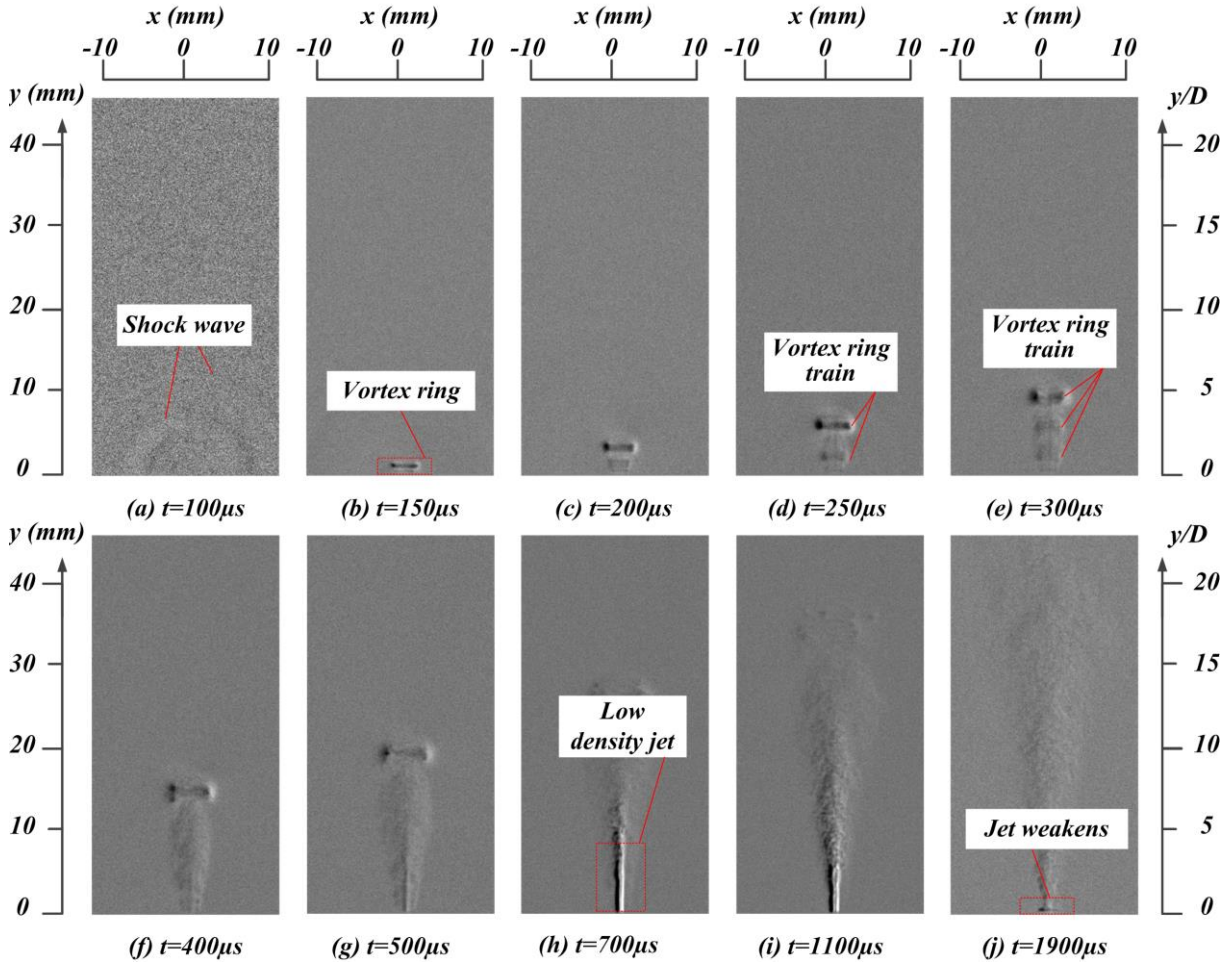

Fig. 6 Schlieren images of the jet evolution for orifice diameter of 2 mm (grayscale values from 0 to 255)

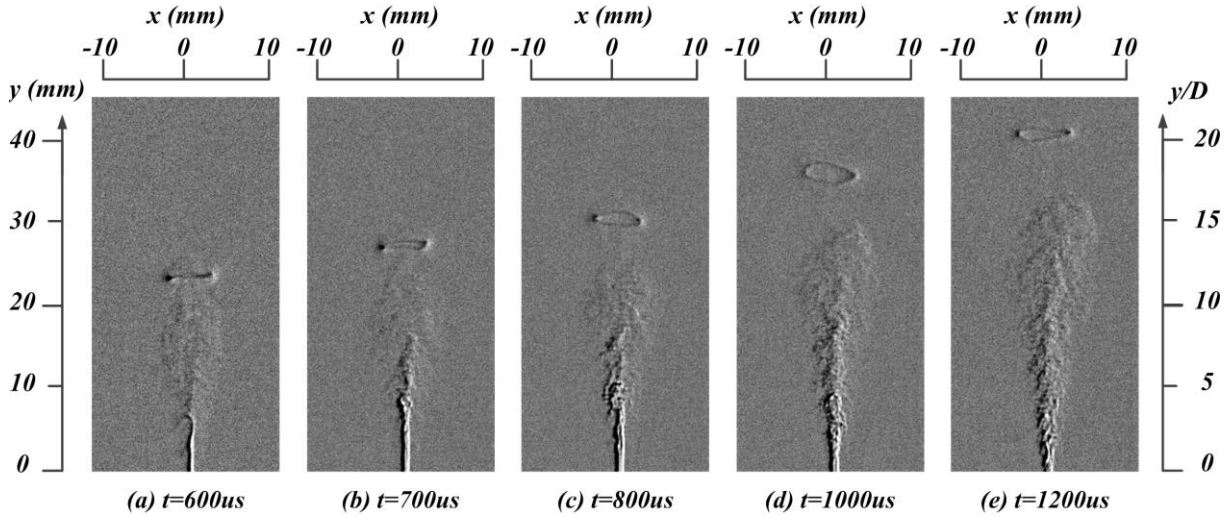

Fig. 7 Vortex ring evolution for orifice diameter of 2 mm (grayscale values from 0 to 255)

B.Vortex ring propagation velocity

Several features extracted from the Schlieren imaging results can be used to estimate the relative influence of the exit orifice diameter on the performance of PSJA. One such feature is the propagation velocity of the front vortex ring formed shortly after the initiation of the discharge. The vortex ring positon is defined as the mid positon between the leftmost and the rightmost point of the vortex core. Based on the detection error (2 pixels) and the frame interval (50 μs), the velocity estimation error is determined to be about 3.7 m/s. The vortex ring propagation velocity (denoted as U_v) is shown in Fig. 8 as a function of exit orifice diameter.

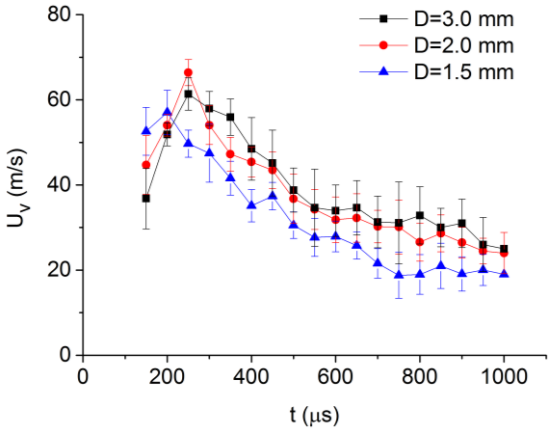

Fig. 8 Evolution of vortex ring propagation velocity

During the evolution of the developing flow field, the vortex ring propagation velocity is governed by an initial linear increase followed by a gradual decrease. The variation trends are similar for all tested diameters. The peak velocity is reached between t = 200 μs and t = 300 μs, ranging from 55 m/s to 70 m/s. Note that this velocity is only half of the maximum jet velocity measured by PIV, as will be shown in Fig. 18.

IV. PIV RESULTS

In the first part of this section, both the averaged velocity fields and the vorticity fields acquired through the PIV measurements are presented. An asymmetry phenomenon is confirmed for the developing jet and the formation mechanism is investigated. In the second part, some important parameters are extracted from the PIV data to quantify the intensity of the three main features pertaining to the developing flow field (shock waves, high speed jet and vortex rings). Further, influence of the orifice diameter is analysed.

A. Flow field evolution

(1). Phase averaged velocity field

The phase averaged velocity (denoted as U_{av}) fields pertaining to the case with a 3 mm diameter are shown in Fig. 9. The jet initiates at t=100 μs, characterised by a relative low velocity (25 m/s). No significant shock wave can be observed at this time. The lack of shock wave seems to be in disagreement with the Schlieren imaging results, where a strong shock wave is observed and no jet issues out at comparable time after discharge. Main reason is that the first expelled gas has a relatively high density (close to the ambient density), which can't be visualized by the schlieren images. In contrast, a clear shock wave structure is observed in several instantaneous PIV flow fields as shown in Fig. 10. The instantaneous velocity is denoted as U_{instan}.

The discrepancy between phase averaged and instantaneous frames is attributed to several factors. Firstly, while the pressure disturbance associated with the shock waves propagates in a supersonic speed, the induced gas motion velocity is quite small (<10 m/s). Additionally, when the flow fields are phase averaged, the sharp edges of the shock waves are smoothened out, due to the disperse of the shockwave location caused by discharge

timing uncertainty. Two evident spherical shock waves are observed, and the induced peak velocities are 2.75 m/s and 0.59 m/s, respectively. When the shock wave propagates away from the exit, its intensity gradually drops, leading to a decreasing induced gas velocity and also a less obvious grayscale variation in Schlieren images. In Section IV.B.(1), the induced peak velocity will be used as an indicator of the shock wave intensity.

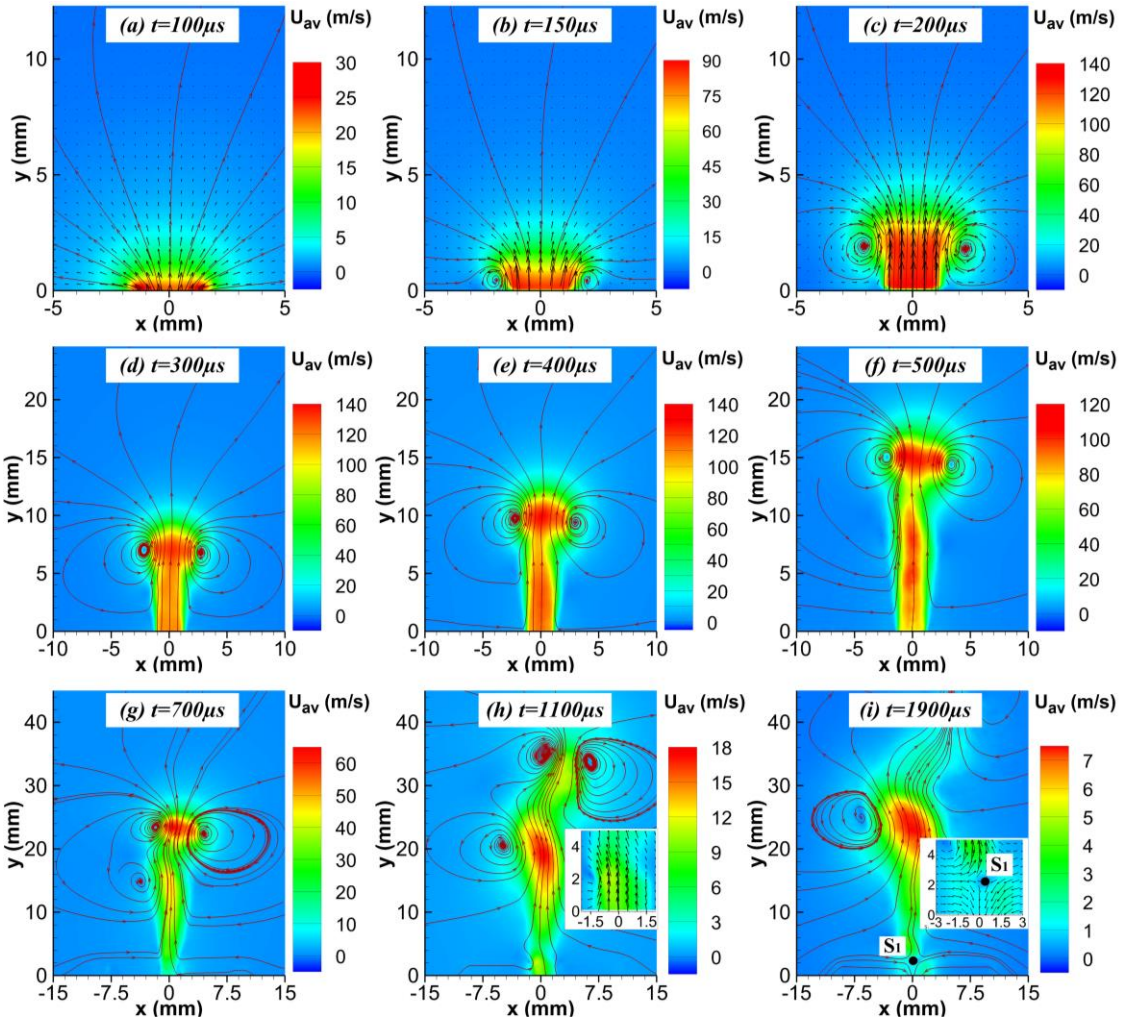

Fig. 9 Phase averaged velocity fields for orifice diameter of 3 mm

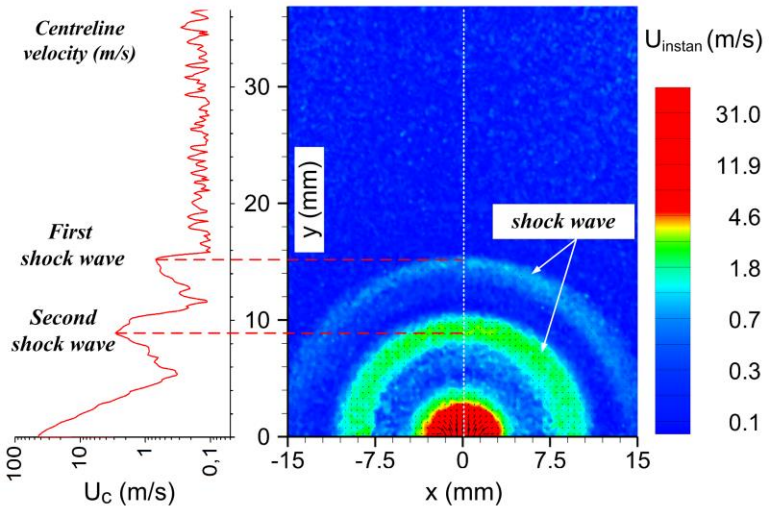

Fig. 10 Instantaneous velocity at t=100 μs (the centerline velocity is arbitrarily offset by 0.1 m/s to facilitate logarithmic scaling)

Resuming the analysis of Fig. 9, at t = 150 μs, a front vortex ring is formed near the exit, which is associated with the rolling of shear layer. As the jet continues, the vortex ring grows in size due to entrainment of surrounding fluid. The vortex ring is characterized by the high velocities in the centre and low speed at the vortex core, which agrees well with the features of Hill's spherical vortex [42]. Additionally, the exit velocity rapidly increases from 30 m/s at t = 100 μs to about 140 m/s (peak jet velocity) at t = 300 μs. Presence of the jet acceleration stage is related with the inertia of throat gas, and the slow energy deposition process (about 400 μs, see Appendix A). Between t = 400 μs and t = 500 μs, the jet core begins to lag behind the front vortex ring, and the exiting jet severs in two separate high velocity regions. This behaviour strikingly differs from the traditional starting jet with constant exit velocity, in which the front spherical vortex is always connected with the jet core and continuously receives momentum input from the jet [39-40].

After t = 700 μs, the topology of the developing flow field exhibits strong asymmetry. The jet core gradually leans to the left hand side, while the front vortex ring leans to the right side during the propagation. This phenomenon agrees well with the schlieren results. Its formation is an unstable process with positive feedback, as shown in Fig. 11. Two factors can trigger the amplification, including the asymmetric vorticity distribution (Stage A), and the non-coaxis between the jet and the vortex ring (Stage B and Stage C).

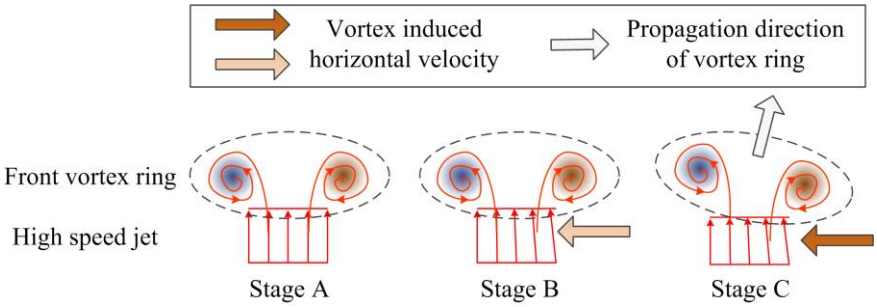

Fig. 11 Conceptual model of the asymmetry amplification process

In stage A, there exists a small difference in the vorticity distribution between the two sides of the vortex pair. Affected by the induced horizontal velocity of vortex pair, the initial vertical jet leans to the left side during propagation (Stage B). This results in one side of the vortex pair receiving higher momentum input than the opposite side. As a result, the left side overtakes the right side, leading to the skewed vortex pair (Stage C). Subsequently, a larger horizontal velocity is produced, and the input momentum of the two sides becomes more uneven. This uneven momentum distribution will further increase the jet skew angle (Stage B). Finally, the vortex pair and the jet separate from each other, and lean to the opposite direction during the propagation (see Fig. 9 (g-i)).

In the case of axisymmetric flow, the asymmetry phenomenon is caused by the skewed jet. As shown in Fig.1 (a), gap between the trigger electrode and the cathode (2 mm), is larger than that between the trigger electrode and the anode (1 mm). Thus, the arc discharge region is not symmetric and so is the pressure distribution in the cavity. Due to the nonuniform pressure distribution in throat inlet and the short throat length (2 mm) used, the jet is ejected with rather small skew angle. As the orifice diameter increases, the "rectification effect" of the throat weakens and the jet skew angle increases. This is analogous to the effect of honeycomb rectifiers in wind tunnels. Finally, an obvious asymmetric flow field is formed in the case of 3 mm orifice diameter.

At t = 1100 μs, a zoomed view of the region near exit is shown. The gas is still issued out from the cavity but with a rather low velocity (<10 m/s). Note that the jet duration time was determined to be approximately 1100 μs by analysis of the Schlieren images. This indicates that density of the issued gas at this time is close to the ambient density, confirming observation by Dufour et al. [41]. At t =1900 μs, the cavity refresh process is observed where air is directed back in the actuator cavity. Due to the suction near the exit orifice, a saddle point (denoted as S1) is observed, which separates the two opposite moving flow regions. The suction velocity is less than 2 m/s, and the suction affected vertical region is about y<2 mm. This means if the plasma synthetic jet (PSJ) is observed at some distance from the exit (larger than 3 mm), no suction can be felt and the PSJ can be regarded as a conventional pulsed jet.

(2). Vorticity field and intensity of velocity fluctuations

The vorticity field and the intensity of fluctuations (rms) of the velocity (denoted as U_{rms}) at different time delays are calculated, as shown in Fig. 12. Q-criterium is used to identify the vortex region and the critical value is chosen as 5 % of the maximum Q value. The identified vortex regions are circled with red lines in the vorticity contour.

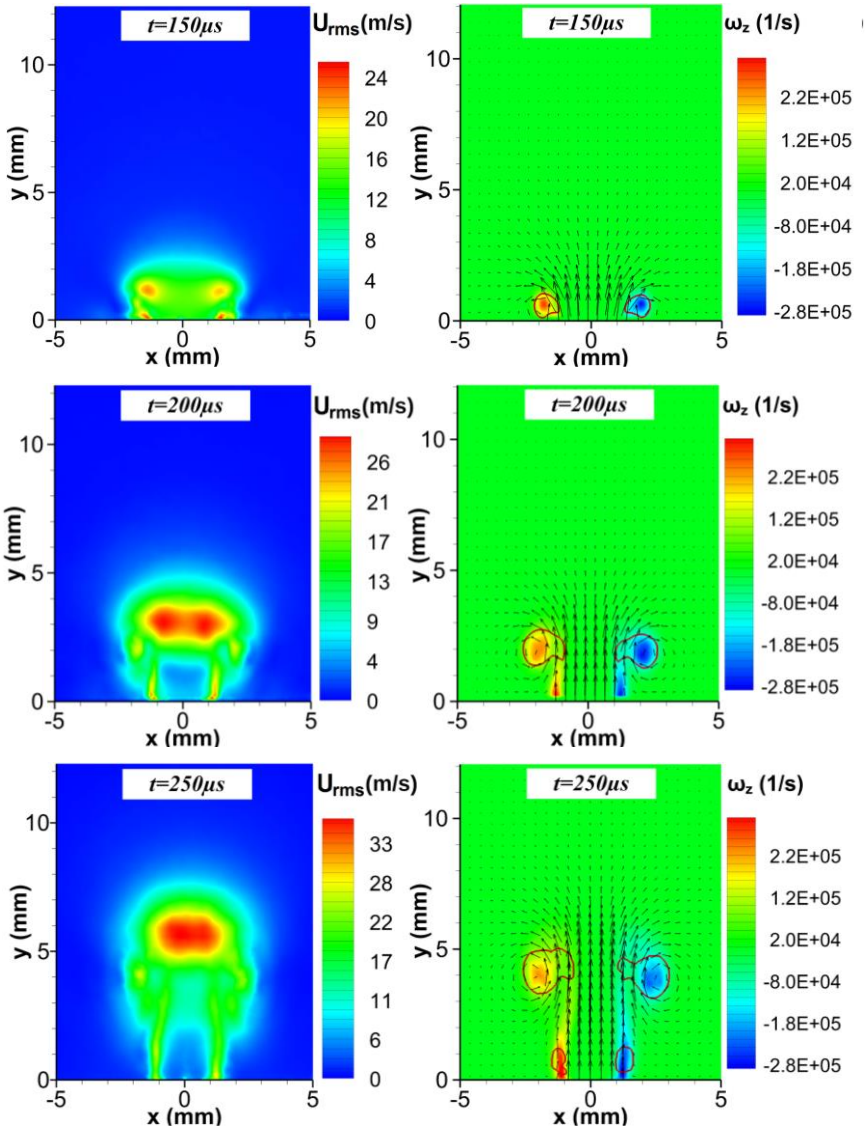

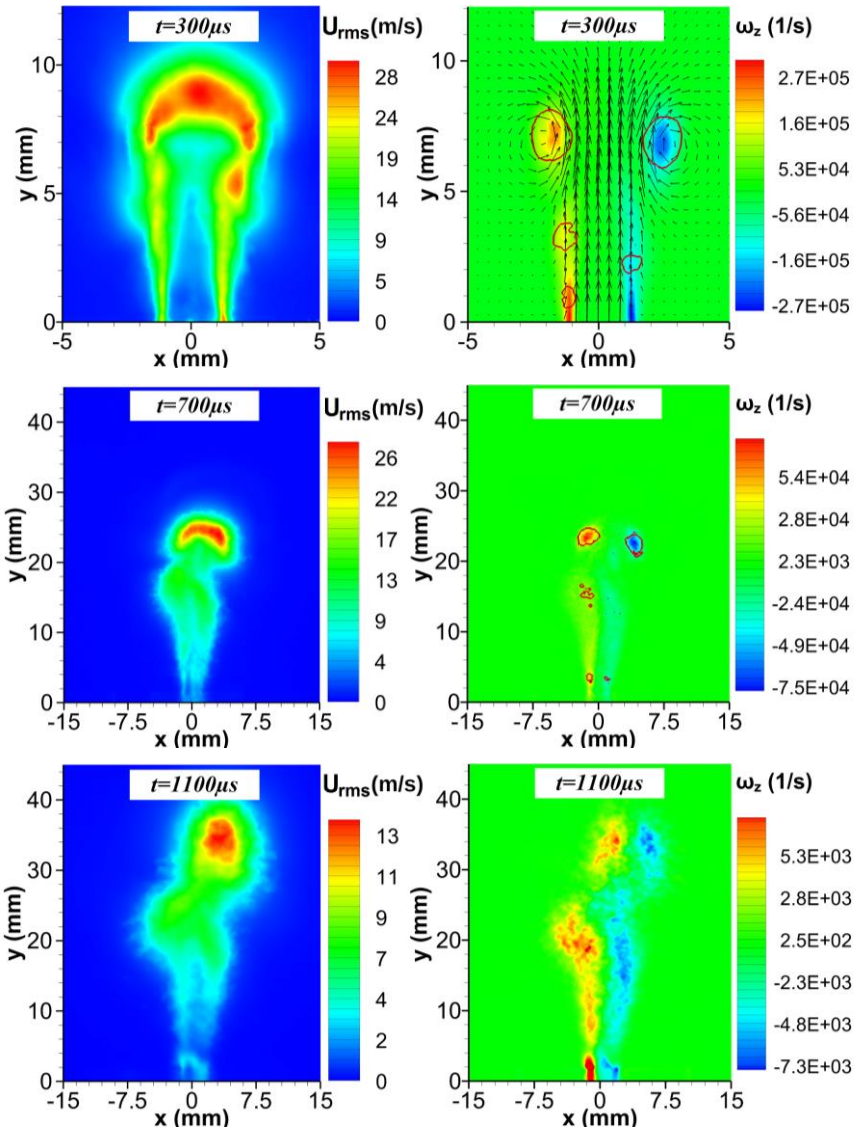

Fig. 12 Evolution of velocity fluctuation and vorticity fields for orifice diameter of 3 mm

At t = 150 μs, the vorticity is mainly concentrated in the front vortex ring. Inner diameter and outer diameter of the front vortex ring are approximately 3 mm and 5 mm, respectively. A large rms is shown near the exit and above the front vortex ring. As the vortex ring propagates downstream, its size grows, entraining more fluid. At t = 200 μs, a strong shear layer is formed, and a large fluctuations are present both in the jet front and in the shear layer, namely the region with high tangential velocity gradient. The Q criterium identifies a well resolved front vortex ring. Additionally, in the jet core, a small rms is observed.

Between t = 250 μs and t = 300 μs, some secondary vortices are identified. They are distributed in the shear layer and demonstrate features of small-scale vortex rings. Formation of this phenomenon is related with the discharge oscillation and can be explained by the boundary vorticity flux (BVF) theory [43-45]. According to BVF theory, vorticity in flow field are created on solid bodies. On an arbitrary solid body, BVF (denoted as $\boldsymbol{\sigma}$) can be expressed as:

$$\boldsymbol{\sigma} = \mathbf{n} \times (\mathbf{a} - \mathbf{f}) + \frac{1}{\rho}[\mathbf{n} \times \nabla P + (\mathbf{n} \times \nabla) \times \mu\boldsymbol{\omega}] \tag{1}$$

With the body force neglected and the actuator kept still, Equation (1) for the 2D flat plate is simplified to the following form:

$$\boldsymbol{\sigma} = \frac{1}{\rho}\mathbf{n} \times \nabla P \Rightarrow \sigma = \frac{1}{\rho}\frac{dP}{dS} \tag{2}$$

where, ρ is gas density; dP/dS is tangential pressure gradient on wall. Actually, Equation (2) doesn't hold for the axisymmetric case. However, considering the thin laser sheet adopted in PIV measurement, the following analysis is still performed in flat plate. Fig. 13 shows vorticity creation in a 2D plasma synthetic jet model.

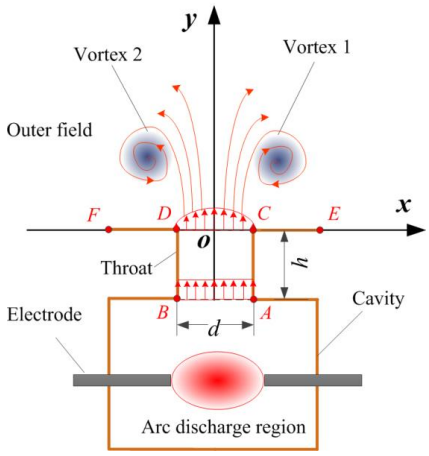

Fig. 13 Conceptual model of vorticity creation in 2D PSJA

Arc discharge induces the pressure increment in cavity, and thus the pressure gradient in actuator throat. Since the jet velocity is subsonic, pressure in the throat exit can be assumed to the ambient pressure and no vorticity are created on the actuator cap (line CE and line DF). Thus, the vorticity in flow field is produced only due to the axial pressure gradient (*oy* direction) in actuator throat. Due to the oscillatory behaviour of the capacitive discharge, both the velocity and the throat pressure oscillate during the jet stage. These oscillations act like some short impulses, which promotes the shedding of small-scale vortex rings.

At t = 700 μs, the front vortex ring can still be observed albeit considerably weakened. Contour of the rms value well depicts the distortion of the jet body, and the maximum rms value still lies in the jet front. After t = 1100 μs, the front vortex ring breaks down, and no intensive vortex can be seen. The vorticity is distributed near the two sides of the jet.

B. Influence of orifice diameter on PSJA performance

(1). Shock wave intensity

As stated in previous section, the shock wave will induce a peak in the profile of centreline velocity (see Fig. 10). This peak velocity indicates the strength of the shock waves. 200 vector fields recorded at t = 100 μs are exploited to extract the shock wave position and also the shock wave induced peak velocity (denoted as V_s). In the case of 3 mm orifice diameter, scatter plots of these two variables are shown in Fig. 14.

In the linear coordinate system, all the scatter points are divided into three categories. Set B corresponds to the case that only one shock wave is presented in the flow field. Set A1 and Set A2 correspond to the case with two shock waves observed, and represent the dataset of the first (front) and the second shock wave, respectively. Due to the rapid attenuation of the gas induced velocity, no case presents three or more shock waves. All the data gathered distribute into two separated regions. In each region the induced gas velocity drops with increasing distance from the wall, indicating a decreasing shock wave intensity. The two regions correspond to two shock waves with different intensities, which are referred as the strong shock wave and the weak shock

wave. At y=2 mm, the induced peak velocities of the two shock waves are about 10 m/s and 5 m/s, respectively. For the weak shock wave, after 16 mm the induced velocity is below 0.5 m/s.

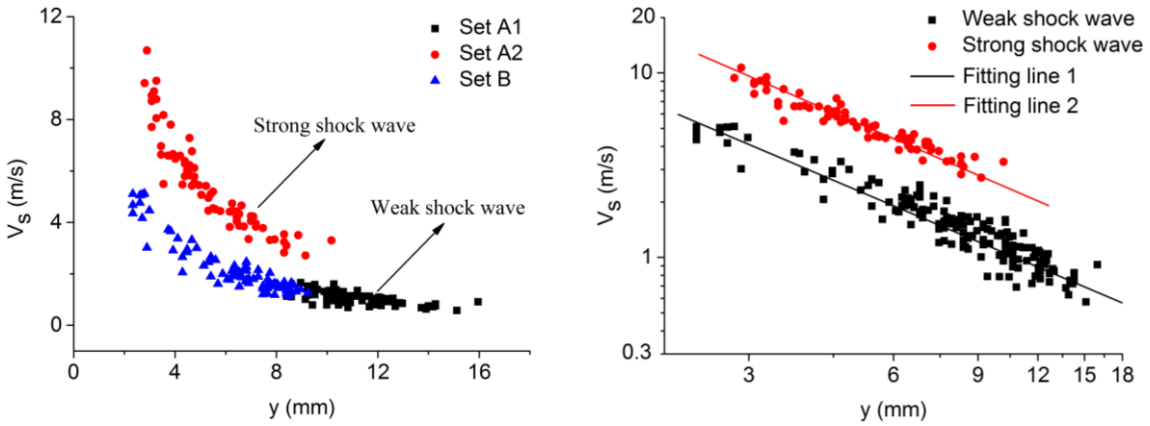

(a) Linear scaling (b) Logarithmic scaling

Fig. 14 Shock wave induced peak velocity as function of shock wave position

It is striking to notice that in the case of two shock waves, the first wave (furthest from the wall) is the weak one, and the second wave is the strong one. However, if only one shock wave is observed, this shock wave must be a weak one. The presence of the double shock waves can be attributed to two effects, shock wave reflection in the cavity and pulsed behaviour of the energy deposition (capacitive discharge). In the case where two shock waves are present, the distance between the strong shock wave and the weak shock wave has a mean value of 5.83 mm and a standard deviation of 0.32 mm. This can exclude the possibility of the shock wave reflection to some extent, since electrodes are located 7.5 mm from the cavity bottom. As such, a reflected wave travelling at approximately similar velocity would have a distance of 15 mm from the primary wave. Thus, it is concluded that the sequential occurrence of the two shock waves is caused by the pulsed behaviour of the discharge (see Appendix A).

Fig 14. (b) illustrates the scatter points in a logarithmic scale. It is clear that a simple power law can be used to describe the induced velocity as function of distance. Using a fitting based on the minimum mean square error (MMSE) method, the following two equations are obtained

$$\begin{cases} V_{s1} = 27.48 y^{-1.306} \\ V_{s2} = 48.87 y^{-1.196} \end{cases} \tag{3}$$

where, V_{s1} and V_{s2} represent the induced peak velocity of the weak and the strong shock wave, respectively. It can be inferred from the above relationship that the induced velocity would become infinite when the distance approaches zero. Naturally, this is not the case. Since the shock wave originates from the orifice, the spherical shock wave is actually evolved from the plane shock wave in actuator throat. After the evolution, diameter of the spherical shock wave should be at least larger than the orifice diameter (3 mm). Hence, lower limit of *y* should be the exit radius (1.5 mm). By substituting this value into Equation (3), the maximum induced gas velocities of the weak and the strong shock wave, are determined to be 16.2 m/s and 30.1 m/s.

Further, as the jet is driven directly by the pressure difference across the actuator throat, the intensity difference of the two shock waves will finally result in the variation of exit velocity. Fig. 15 shows the distribution of the exit velocity (denoted as V_e) among the 200 PIV realisations.

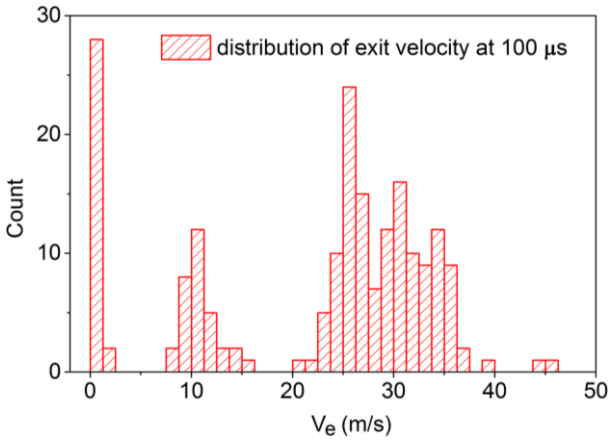

Fig. 15 Histogram of the exit velocity distribution at t=100 μs

Overall, the exit velocities mainly distribute in three intervals, [0, 3], [7, 17] and [20, 40]. The first interval [0, 3] is resulting from the cases in which neither shock wave nor jet are present in the flow field. Ranges of the other two intervals cover the calculated maximum induced velocities (16.2 m/s and 30.1 m/s) of the two shock waves. This indicates that each issue of the shock wave is followed by the ejection of cavity gas. The intensity of the shock wave is proportional to the induced exit velocity.

In order to further compare the influence of orifice diameter, the velocity induced by the strong shock wave (raw data in Set A2) is averaged in a sequence of intervals with a fixed length of 0.5 mm. These intervals start from 1.5 mm to 5.5 mm, and have no overlap with each other. With different orifice diameters, variations of the averaged velocity are shown in Fig. 16.

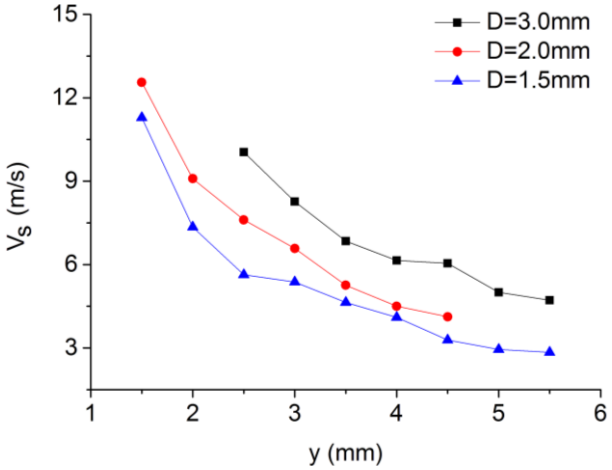

Fig. 16 Variation of the averaged shock wave induced velocity

In the case of 3 mm diameter, no data are available at distances below 2 mm. Comparing the averaged induced velocity at same location, it becomes evident that the intensity of the shockwave is proportional to the exit orifice diameter. Between 2.5 mm and 5.5 mm, the averaged velocity with a 3 mm diameter are always approximately twice of that with a 1.5 mm diameter. This can be explained as follows. With the same energy deposition and cavity geometry, change of the orifice diameter doesn't affect the shock wave evolution within the cavity. Thus, for the three tested diameters, the plane shock waves in the orifice throat can be assumed as possessing similar energy per unit area. Total mechanical energy incorporated in the plane shock wave is proportional to the throat area. As the spherical shock wave is evolved from the plane shock wave, its intensity

(mechanical energy) is also lineraly proportional to the exit area. Consequently, the induced velocity in same location is proportional to the orifice diameter.

(2). Exit velocity

The measured PIV velocity fields provide access to the intensity, duration and evolution of the high speed jet developing shortly after the energy deposition in the PSJA cavity. The high speed jet is the primary flow control mechanism associated with the PSJA . In order to quantify the jet intensity, the averaged exit velocity is extracted, and the region used to average is a rectangular area just above the exit, with the width set as half of the orifice diameter and the height fixed as 0.5 mm. In the case of 2 mm orifice diameter, variation of the averaged exit velocity with time is shown in Fig. 17. For comparison, the averaged grayscale difference obtained from the Schlieren results is presented.

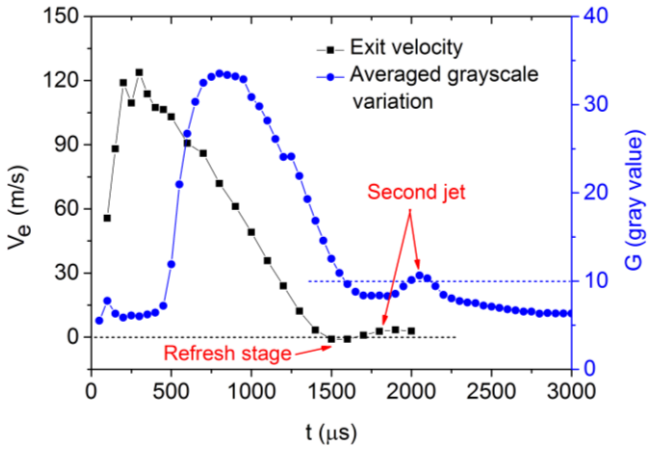

Fig. 17 Evolution of jet exit velocity for orifice diameter of 2 mm

Comparing the two curves shown in Fig. 17, the variation trends are similar, but a time lag between PIV and Schlieren observation is evident. In one period, the exit velocity shows first a sharp increase and then a gradual decrease. At t = 100 μs a weak jet with a velocity of 50 m/s, is expelled out, closely following the issue of shock waves. Between t = 100 μs and t = 200 μs, the jet accelerates, and the velocity increases linearly from 50 m/s to 120 m/s. Presence of the jet acceleration stage is due to the relative long discharge duration (about 300 μs). Between t =200 μs and t =500 μs, the velocity is sustained to high values and oscillates around 120 m/s. However, the high velocity at this stage is not reflected in the averaged grayscale variation. This illustrates again that heating of the arc discharge is rather nonuniform in space, and the initially expelled air is of rather ambient density near the exit. After t = 500 μs, the exit velocity gradually drops, also in a linear way.

At t = 1.5 ms, a weak negative exit velocity (-0.88 m/s) is observed, indicating the occurrence of the refresh stage. Thus, duration of the first jet stage is estimated to be 1.4 ms. After a very short refresh stage (about t = 100 μs), a second jet is presented with a very low velocity (about 3 m/s). Although no PIV experiments are performed after t = 2 ms in the case of 2 mm diameter, it can still be concluded that in a whole period, the jet stage and the refresh stage will occur more than once. In [23], this phenomenon has already been predicted by the analytical model. However, the suction velocity is much smaller than that predicated in [23] (about 30 m/s). Additionally, the second jet is also observed in the grayscale variation, while its occurrence is later (2 ms).

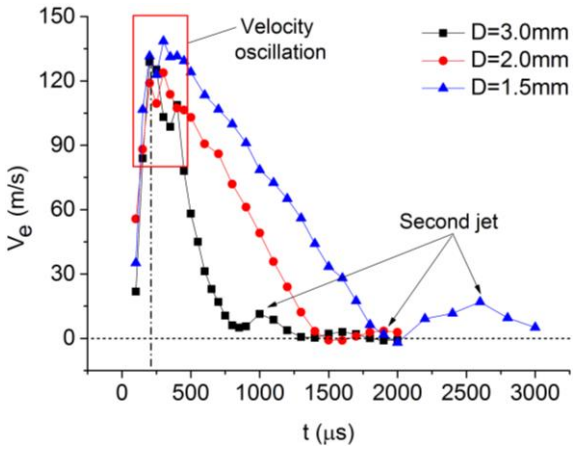

Fig. 18 Influence of orifice diameter on the evolution of exit jet velocity

Variations of the exit velocity with different orifice diameters are shown in Fig. 18. Variation trends in the case of different diameters, are quite similar. As the diameter decreases, the curve extends along the horizontal axis, with the maximum velocity changing slightly around 130 m/s. The most dominant effect associated with the orifice diameter is the jet duration. With a diameter of 3 mm, the first jet is sustained until 2 ms. In the case of 3 mm diameter, three jet stages are present, and no refresh stage (negative exit velocity) is observed between the first and the second jet stage. If the termination of the first jet stage is defined at the first minimum of the exit velocity, the jet duration is estimated to be 0.85 ms. Peak velocities of the second jet stage with the diameter of 3 mm and 1.5 mm, are 17 m/s and 11 m/s, respectively. However, they are still significantly weaker compared with that of the first jet stage. Considering this difference and also the short duration, other jet stages, except for the first one, can be neglected for purposes of simplified PSJA modelling.

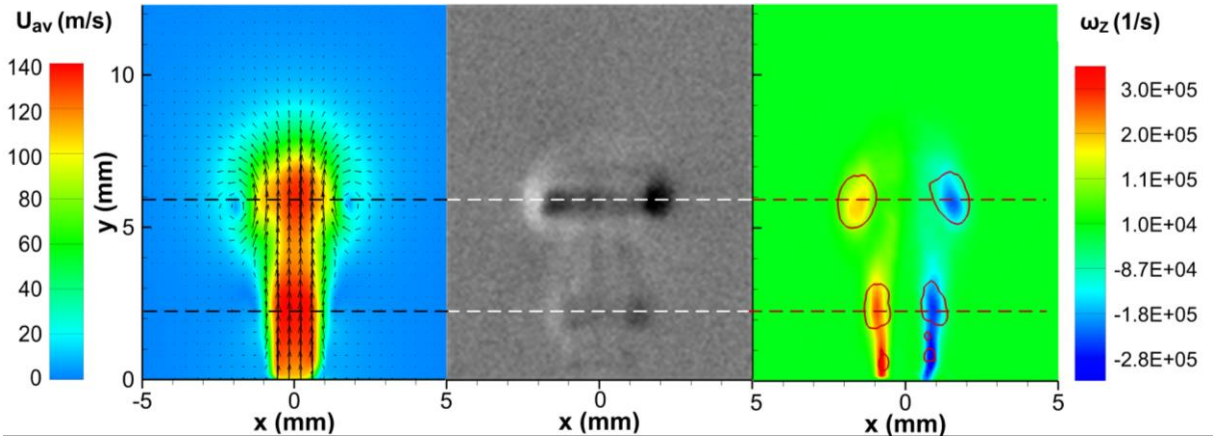

Fig. 19 Velocity field, Schlieren image and vorticity field at t=250 μs for orifice diameter of 2 mm

An important feature of the evolving jet in Fig. 18 is the velocity oscillation between t = 200 μs and t = 400 μs. This is directly related with the formation of the vortex ring train shown in Fig. 6 (e) and Fig. 12 (d), and also the alternate presence of the high and low speed region. Fig. 19 shows a comparison of the velocity field, the vorticity field and also the schlieren image, at t = 250 μs in the case of 2 mm diameter.

In the velocity field, two high speed regions are observed. With one in the centre of front vortex ring, and the other between the exit and the front vortex ring. By using Q-criterium, some vortices are identified, and the positions agrees quite well with the dark region in schlieren images. This phenomenon indicates some close connections between the high-speed regions and the vortex rings. To confirm this conjecture, the vertical

velocity in actuator centreline, the horizontal-averaged grayscale and the horizontal-averaged Q value, are extracted and shown in Fig. 20. Note that the vertical scale of the middle plot is descending.

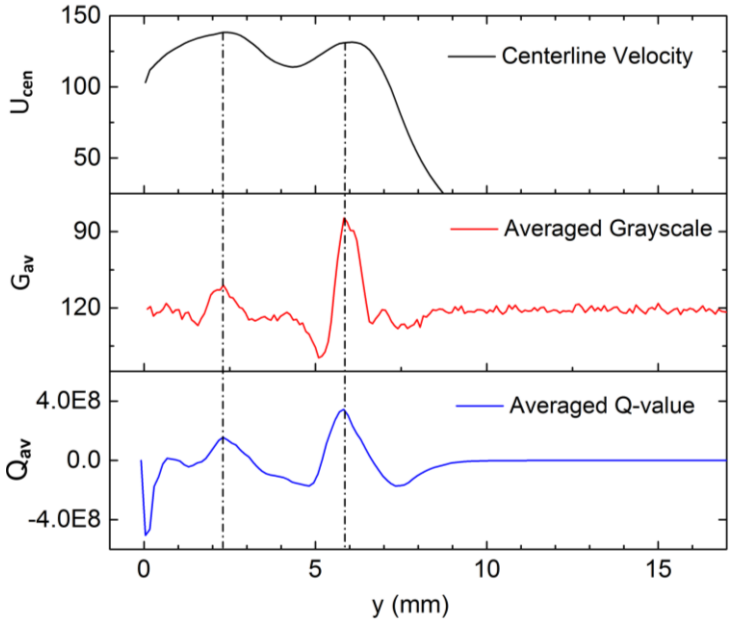

Fig. 20 Centerline velocity, horizontal-averaged grayscale and horizontal-averaged Q-value for orifice diameter of 2 mm.

Peak positions of the three curves show a rather good agreement at 2.3 mm and 5.8 mm. Association between the high speed regions and the vortex rings, can be explained with the BVF theory. Due to the oscillatory nature of the capacitive discharge, the pressure in throat inlet oscillates in a similar manner. Pressure difference between the throat inlet and the throat outlet is the driving force of the jet. With the pressure at the throat outlet assumed as the ambient pressure, an oscillating inlet pressure will result in an oscillating exit velocity, as shown in Fig. 18. Additionally, as the jet propagates along the axisymmetric axis, this oscillating behaviour is projected on the spatial evolution of the jet and reflected as the alternate occurrence of the high and low speed regions (see Fig. 21 (b)).

From the point view of vorticity, axial pressure gradient in the actuator throat is linearly proportional to the BVF. A pressure peak at the throat inlet leads to the creation of a high vorticity region in the throat boudary layer, which finally rolls into a vortex ring after being shed from the exit. Thus, the high speed regions and the vortex rings (high vorticity regions) are formed simultaneously, due to the same strong pressure oscillation in the throat inlet. It should be noted that the generated vorticity is proportional to both the pressure gradient and also the duration, namely the integration of the pressure gradient to the time. In contrast, for the initial fast propagating shock waves, no vortex ring will be induced due to the short duration.

The oscillatory behaviour of the jet and the formation of vortex ring train, are more obvious in the case of 1.5 mm diameter, as shown in Fig. 21. In Fig. 21 (b), four high speed regions are observed in the core of the jet with almost uniform spatial distribution, indicating that the pressure oscillation in throat inlet is periodic. By analyzing the vorticity field (vortex ring numbers) shown in Fig. 12 and Fig. 21, the generation rate of the vortex rings is estimated to be approximately 50 μs per vortex ring. This illustrates the pressure oscillation period is also about 50 μs, which agrees well with the periodical behaviour of the discharge waveforms (see Appendix A). Thus, the pressure oscillation in throat inlet, caused by the pulsed energy deposition, is the root of the intermittent presence of high-speed regions, and also the train of vortex rings.

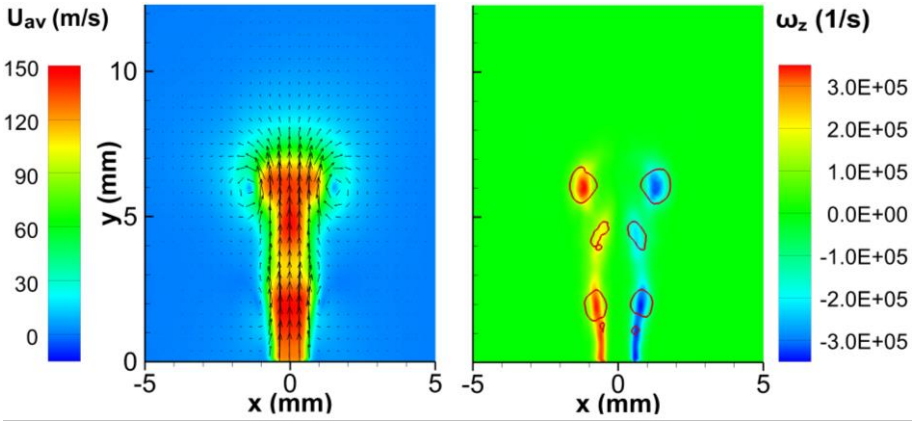

(a) t=250 μs, D=1.5 mm

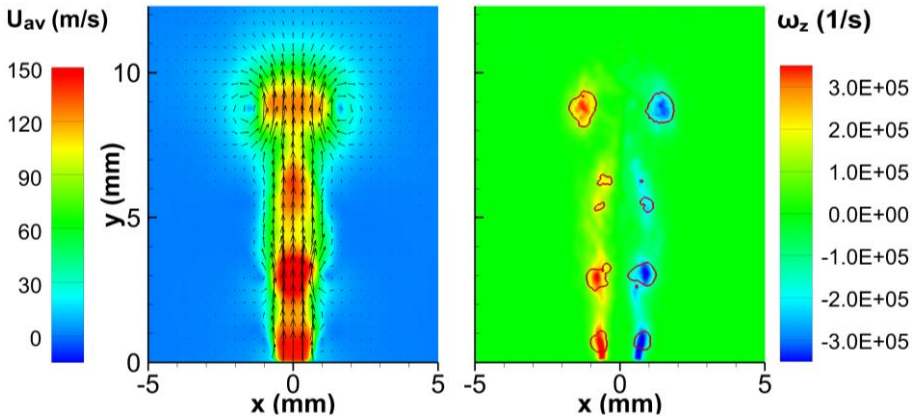

(b) t=300 μs, D=1.5 mm

Fig. 21 Velocity and vorticity fields for orifice diameter of 1.5 mm

(3). Front vortex ring

According to the previous discussion, the front vortex ring plays an important role in the flow field evolution. In order to investigate its motion characteristics, the front vortex ring is first identified with the Q criterium. The threshold value is chosen as 1000 s^{-2} instead of 0 s^{-2}, in order to mitigate background noise effects. A preliminary sensitivity study indicates that for threshold value changing from 100 s^{-2} to 10000 s^{-2}, relative variation of the results presented in the following figures is less than 2%. Denote the positive vorticity distribution of the vortex ring (left half part) as $\omega_+(x,y)$. Then, centre coordinates of the left half part, (x^+, y^+), are determined as follows.

$$\begin{cases} x^+ = \dfrac{\iint \omega^+(x,y)\cdot x dS}{\iint \omega^+(x,y)\cdot dS} \\ y^+ = \dfrac{\iint \omega^+(x,y)\cdot y dS}{\iint \omega^+(x,y)\cdot dS} \end{cases} \tag{4}$$

By analogy, centre coordinates of the right part (x^-, y^-) can also be obtained. By virtue of this two coordinates, vortex ring diameter, and vortex ring centre location (defined as the mid of the left and the right part centre coordinate) are calculated and tracked in time. Fig. 22 shows the temporal evolution of the vertical location, and the centre locations.

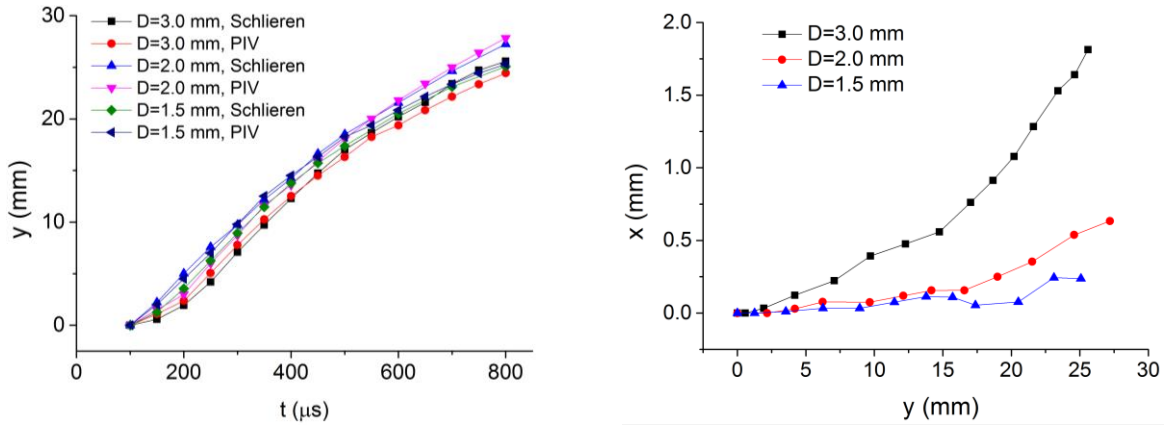

(a). Temporal evolution of the vertical location (b) Spatial evolution of the centre location

Fig. 22 Motion of front vortex ring

In Fig. 22 (a), the vertical position obtained with PIV agrees well with the respective Schlieren results. This illustrates that the generated oil particles used for PIV seeding can follow accurately the high speed jet. As front vortex ring propagates downstream, the curve slope decreases, indicating a declining propagation velocity. Maximum propagation distance of the front vortex ring exceeds 25 mm in the quiescent conditions of this study. In Fig. 22 (b), centre of the front vortex ring are not always lies in the actuator centreline. Actually, all the traces lean to the positive *ox* direction. As the orifice diameter increases, deviation of the vortex ring centre to the axis also increases. This is caused by the asymmetry electrode configuration, as explained in Section IV.A.(1). A large diameter leads to a weak rectification effect, and finally a large deviation to the actuator centreline.

Fig. 23 shows the variation of the vortex ring diameter (denoted as D_v). With increasing exit orifice diameter, the initial diameter of the shed vortex ring also increases. As the vortex ring propagates downstream, its diameter further increases. The enlargement rate remains almost constant before y = 20 mm, and has no relationship with the orifice diameter. After 20 mm, the front vortex ring diameter in the case of 3mm diameter begins to drop, while the diameters in other two cases keep increasing linearly. This is attributed to the large deviation in the propagation directions of the vortex ring and the high speed jet, in the case of 3 mm diameter. Deviation in the propagation direction leads to the sharp decreasing of the momentum input of the vortex ring, and finally the shrinking of the front vortex ring.

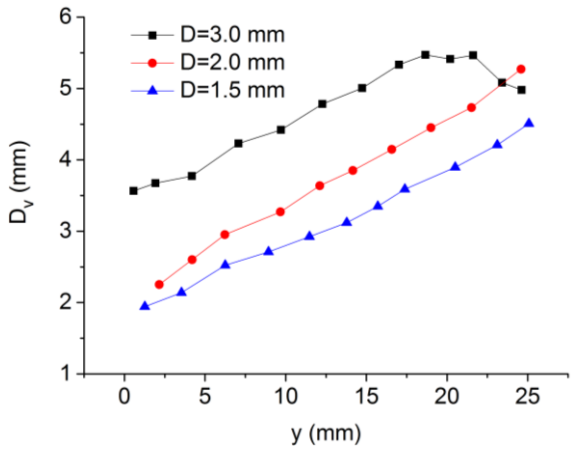

Fig. 23 Variation of the vortex ring diameter

Additionally to the motion parameters, circulation can also be used to characterise the front vortex ring. Calculation of the circulation (denoted as Γ) is shown as follows.

$$\Gamma = 0.5 \cdot \left[\iint \omega^{+}(x,y) \cdot dS + \iint \left| \omega^{-}(x,y) \right| \cdot dS \right] \tag{6}$$

Fig. 24 shows the variation of the total circulation of the front vortex ring.

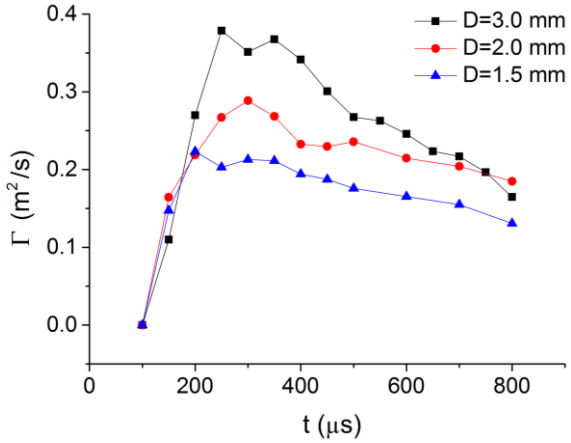

Fig. 24 Circulation of the front vortex ring

Within one period, circulation of the front vortex ring first increases linearly and then decreases gradually. Prior to t = 200 μs, the starting vortex intensity is insensitive to variations of orifice diameter. Presence time of the peak vortex tube intensity varies between t=200 μs and t=300 μs. As the diameter increases, peak value of the vortex tube intensity goes up, indicating a rising vortex ring intensity.

V. CONCLUSIONS

In this work, a sequential discharge power supply system is designed based on a high-voltage amplifier, to accommodate a three-electrode, large-volume PSJA. Characteristics of PSJA in quiescent flows are investigated with high-speed Schlieren imaging system and two-component phase-locked PIV system. Some distinctive phenomena, including the asymmetry of the developing flow field and the formation of a vortex ring train, are observed. Intensity of the three primary features (shock waves, high-speed jet and front vortex ring), are compared for cases of different orifice diameters.

With a 3 mm orifice diameter, a distinct asymmetric flow field is presented, where the front vortex ring and the high speed jet lean in opposite directions during their propagation. Development of the asymmetric flow field is an unstable process with positive feedback. Misalignment between the vortex ring and the jet, caused by the asymmetric electrode configuration, triggers the amplification process. As the orifice diameter decreases, rectification effect of the throat strengthens and the asymmetry phenomenon is largely mitigated.

In the vorticity field, a train of vortex rings, distributed uniformly along the actuator axis, is observed. Each vortex ring has a corresponding high-speed region in its centre. Reedy et al. also obtains this phenomenon in the case of low energy deposition [19]. Root of their formation is the periodic pressure oscillation in the throat inlet, inherently present in the capacitive arc discharge. The alternate occurrence of high and low speed regions is more pronounced in the case of small exit orifice diameter.

Two kinds of shock waves with varied intensities are issued from the cavity exit, shortly after discharge. The strong shock wave always precedes the weak one. A velocity perturbation typically less than 10 m/s is induced due to the shock waves. As the distance to exit increases, the shock wave induced velocity decays. Intensity of the strong shock wave is positively proportional to the orifice diameter.

Regarding the high-speed jet, there exists more than one jet stage and one refresh stage per actuation cycle, as predicted by the analytical model in Zong et al. [23]. In the first jet stage, the exit velocity first increases sharply, then oscillates around the peak value and finally drops linearly. Density of the initially expelled gas is the cool air of rather ambient density, whereas the later ejected gas is the low-density hot air directly heated by arc discharge. Orifice diameter has no influence on the jet acceleration stage and the peak exit velocity (around 130 m/s). However, a large diameter results in a rapid decline of jet velocity and thus a short jet duration time, as observed in Zong et al. [33].

Propagation velocity of the front vortex ring reaches values of approximately half the peak exit velocity. Influence of orifice diameter on the vortex ring propagation velocity is not as significant as that on jet exit velocity. In the case of 3 mm orifice diameter, trajectory of the vortex ring severely deviates from the actuator axis of symmetry. Initial diameter of the vortex ring is positively proportional to the orifice diameter, and increases almost linearly with the propagation distance. Circulation of the front vortex ring shows a similar variation to the propagation velocity. A large orifice diameter results in a high peak circulation.

To summarize, shock waves, high speed jet and vortex rings are the three main features of the induced flow field of PSJA. Increase of the orifice diameter leads to more vigorous actuation effects but reduces their duration. The three primary flow structures, induced by the PSJA, are expected to contribute to a certain extent to the combined control authority of this type of actuators. Their relative importance is naturally expected to be a function of the strength and nature of the external flow. Future work by the authors will concentrate on the influence of the external flow on the performance of this actuator

APPENDIX A: Electrical measurements

In order to gain insight in the oscillatory behaviour of the capacitive discharge, the voltage drop on the connecting wire between the capacitor cathode and the ground (denoted as V_{wire}), is first measured with a voltage probe (Philips, PM 8926/59), and then recorded by an oscilloscope (Tektronix, TDS 3054C) at 25 MHz recording rate. A qualitative illustration of the periodic behaviour of the energy deposition, and the discharge timescale is shown in Fig. A1.

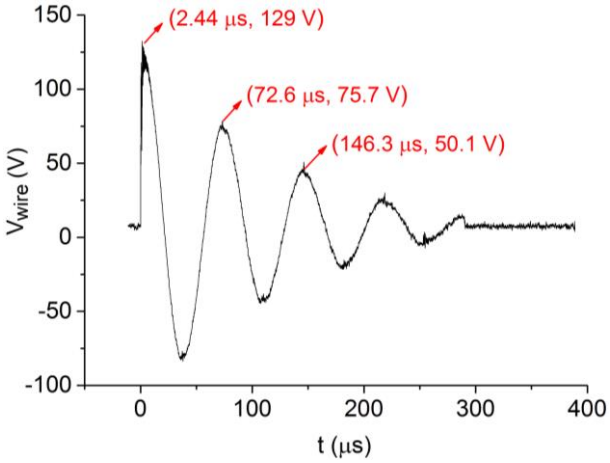

Fig. A1 Voltage waveform

The present waveform approximately reflects the variation law of the discharge current, to some extent. In one period, the discharge current oscillates with decreasing amplitude. With the arc region simplified as a resistor, the energy deposition is proportional to the square of the discharge current. Thus, the energy deposition

will also behave in a periodic way, and the pulse period should be half of the current oscillation period [33]. Based on the three peaks marked in Fig. A1, oscillation period of the energy deposition is estimated to be 36 μs.

Additionally, a total of 9 peaks are observed while the total discharge duration is about 300 μs. This discharge duration is much longer than that observed in Belinger et al. [22]. Characteristic time of discharge is determined by the product of total capacitance and total inductance in discharge circuit. In our experiments, the capacitance is 1 μF, much larger than that used by Belinger et al (20 nF). This difference in capacitance, together with the parasitic inductance in our capacitor, finally results in a much longer discharge duration.

REFERENCES

[1]. Cattafesta L N, Sheplak M. Actuators for active flow control. Annual Review of Fluid Mechanics, 2011, 43: 247-272

[2]. Corke T C, Enloe C L, Wilkinson S P. Dielectric barrier discharge plasma actuators for flow control. Annual Review of Fluid Mechanics, 2010, 42: 505-529

[3]. Li Y H, Wu Y, Li J. Review of the investigation on plasma flow control in China. International Journal of Flow Control, 2012, 4(1+2): 1-17

[4]. Kotsonis M, Giepman R, Hulshoff S, et al. Numerical study of the control of tollmien–schlichting waves using plasma actuators. AIAA Journal, 2013, 51(10):2353-2364

[5]. Bletzinger P, Ganguly B N, Van W D, et al. Plasmas in high speed aerodynamics. Journal of Physics D: Applied Physics, 2005, 38(4): R33–R57

[6]. Webb N, Clifford C, Samimy M. Control of oblique shock wave/boundary layer interactions using plasma actuators. Experiments in Fluids, 2013, 54(6): 1545

[7]. Popkin S H, Taylor T M, Cybyk B Z. Development and application of the plasma synthetic jet actuator for high-speed flow control. Johns Hopkins APL Technical Digest, 2013, 32(1): 404-419

[8]. Narayanaswamy V, Rajia L, Clemens N T. Control of unsteadiness of a shock wave/turbulent boundary layer interaction by using a pulsed-plasma-jet actuator. Physics of Fluids, 2012, 24: 076101

[9]. Greene B R, Clemens N T, Magari P, et al. Control of mean separation in shock boundary layer interaction using pulsed plasma jets. Shock waves, 2015, 25:495-505

[10]. Emerick T, Ali M Y, Foster C, et al. Sparkjet characterizations in quiescent and supersonic flow fields. Experiments in Fluids, 2014, 55: 1858

[11]. Caruana D, Rogier F, Dufour G, et al. The plasma synthetic jet actuator, physics, modeling and flow control application on separation. Aerospace Lab, 2013:1-13

[12]. Caruana D, Barricau P, Hardy P, et al. The “plasma synthetic jet” actuator aero-thermodynamic characterization and first flow control applications. AIAA 2009-1307

[13]. Anderson K, Knight D. Plasma jet for flight control. AIAA Journal, 2012, 50(9): 1855-1873

[14]. Cybyk B Z, Grossman K R, Wilkerson J T, et al. Single-pulse performance of the sparkjet flow control actuator. AIAA 2005-401

[15]. Haack S J, Taylor T, Emhoff J, et al. Development of an analytical plasma synthetic jet model. AIAA 2010-4979

[16]. Hardy P, Barricau P, Belinger A, et al. Plasma synthetic jet for flow control. AIAA 2010-5103

[17]. Zong H H, Cui W, Wu Y, et al. Influence of capacitor energy on performance of a three-electrode plasma synthetic jet actuator. Sensors and Actuators A: Physical, 2015, 222:114–121

[18]. Wang L. Xia Z X, Luo Z B, et al. Three-electrode plasma synthetic jet actuator for high-speed flow control. AIAA Journal, 2014, 52(4): 879-882

[19]. Reedy T M, Kale N V, Dutton J C, et al. Experimental characterization of a pulsed plasma jet. AIAA Journal, 2013, 51(8): 2027-2031

[20]. Shin J. Characteristics of high speed electro-thermal jet activated by pulsed DC discharge. Chinese Journal of

Aeronautics, 2010, 23(5): 518-522
[21]. Belinger A, Hardy P, Gherardi N, et al. Influence of the spark discharge size on a plasma synthetic jet actuator. IEEE Transactions on Plasma Science, 2011, 39(11): 2334-2335
[22]. Belinger A, Naude N, Cambronne J P, et al. Plasma synthetic jet actuator: electrical and optical analysis of the discharge. Journal of Physics D: Applied Physics, 2014, 47: 245202
[23]. Zong H H, Wu Y, Li Y H, et al. Analytic model and frequency characteristics of plasma synthetic jet actuator. Physics of Fluids, 2015, 27:027105
[24]. Sary G, Dufour G, Kourtzanidis K. Modeling and parametric study of a plasma synthetic jet for flow control. AIAA Journal, 2014, 52(8): 1591-1603
[25]. Narayanaswamy V, Rajia L, Clemens N T. Characterization of a high-frequency pulsed-plasma jet actuator for supersonic flow control. AIAA Journal, 2010, 48(2): 297-305
[26]. Belinger A, Hardy P, Barricau P, et al. Influence of the energy dissipation rate in the discharge of a plasma synthetic jet actuator. Journal of Physics D: Applied Physics, 2011, 44: 365201
[27]. Haack S J, Taylor T, Cybyk B Z. Experimental estimation of sparkjet efficiency. AIAA 2011-3997
[28]. Golbabaei-Asl M, Knight D, Anderson K, et al. SparkJet efficiency. AIAA 2013-0928
[29]. Golbabaei-Asl M, Knight D, Wilkinson S. Novel technique to determine Sparkjet efficiency. AIAA Journal, 2015, 53: 501-504
[30]. Zhu Y F, Wu Y, Jia M, et al. Influence of positive slopes on ultrafast heating in an atmospheric nanosecond-pulsed plasma synthetic jet. Plasma Sources Science and Technology, 2015, 24:015007
[31]. Xu D A, Shneider M N, Lacoste D A, et al. Thermal and hydrodynamic effects of nanosecond discharges in atmospheric pressure air. Journal of Physics D: Applied Physics, 2014, 47: 235202
[32]. Cybyk B Z, Wilkerson J T, Grossman K R, et al. Computational assessment of the sparkjet flow control actuator. AIAA 2003-3711
[33]. Zong H H, Wu Y, Song H M, et al. Influence of geometric parameters on performance of plasma synthetic jet actuators. Journal of Physics D: Applied Physics, 2016, 49(2):025504
[34]. Zhang Z B, Wu Y, Jia M, et al. Influence of the discharge location on the performance of a three-electrode plasma synthetic jet actuator. Sensors and Actuators A: Physical, 2015, 235:71-79
[35]. Wang L, Xia Z X, Luo Z B, et al. Effect of pressure on the performance of plasma synthetic jet actuator. Science China-Physics, Mechanics & Astronomy. 2014, 57(12):2309-2315
[36]. Haak S J, Land H B, Cybyk B Z. Characterization of a high-speed flow control actuator using digital speckle tomography and PIV. AIAA 2008-3759
[37]. Ko H S, Haack S J, Land H B, et al. Analysis of flow distribution from high-speed flow actuator using particle image velocimetry and digital speckle tomography. Flow Measurement and Instrumentation, 2010, 21: 443–453
[38]. Laurendeau F, Chedevergne F, Casalis G. Transient ejection phase modeling of a plasma synthetic jet actuator. Physics of Fluids, 2014, 26:125101
[39]. Cantwell B J. Viscous starting jets. Journal of Fluid Mechanics. 1986, 173:159-189
[40]. Pullin D L. Vortex ring formation at tube and orifice openings. Physics of Fluids, 1979, 22(3):401-403
[41]. Dufour G, Hardy P, Quint G, et al. Physics and models for plasma synthetic jets. International Journal of Aerodynamics, 2013, 3:47-70
[42]. Wu J Z, Ma H Y and Zhou M D. Vorticity and vortex dynamics, Springer, Berlin, 2007, Chap. 6
[43]. Wu J Z and Wu J M. Vorticity dynamics on boundaries. Advances in Applied Mechanics, 1996, 32:119-275
[44]. Wu J Z and Wu J M. Interaction between a solid surface and a viscous compressible flow field. Journal of Fluid Mechanics, 1993, 254:183-211
[45]. Yen J and Ahmed N A. Synthetic jets as a boundary vorticity flux control tool, AIAA Journal, 2013, 51(2):510-513